ACS APPLIED MATERIALS & INTERFACES

Research Article

Cite This: ACS Appl. Mater. Interfaces 2019, 11, 22129−22140

www.acsami.org

Biocompatible Two-Dimensional Titanium Nanosheets for Multimodal Imaging-Guided Cancer Theranostics

Zhongjian Xie,[†,¶] Shiyou Chen,[†,¶] Yanhong Duo,[†,¶] Yao Zhu,[†,¶] Taojian Fan,[†,¶] Qingshuang Zou,[†,‡] Mengmeng Qu,[§] Zhitao Lin,[†] Jinlai Zhao,[⊥,#] Yang Li,[‡] Liping Liu,[*,‡] Shiyun Bao,[‡] Hong Chen,[*,∥] Dianyuan Fan,[‡] and Han Zhang[*,†]

[†]SZU-NUS Collaborative Innovation Center for Optoelectronic Science & Technology, International Collaborative Laboratory of 2D Materials for Optoelectronics Science and Technology of Ministry of Education, College of Physics and Optoelectronic Engineering, Shenzhen University, Shenzhen 518060, China

[‡]Department of Hepatobiliary and Pancreatic Surgery, Shenzhen People's Hospital, Second Clinical Medical College of Jinan University, Shenzhen, Guangdong Province 518208, P. R. China

[§]Research Center for Clinical & Translational Medicine, Beijing 302 Hospital, Beijing 100039, China

[∥]School of Materials Science and Energy Engineering, Foshan University, Foshan 528000, China

[⊥]Faculty of Information Technology, Macau University of Science and Technology, Avenida Wai Long, Taipa 999078, Macau, P. R. China

[#]College of Materials Science and Engineering, Shenzhen Key Laboratory of Polymer Science and Technology, Guangdong Research Center for Interfacial Engineering of Functional Materials, Shenzhen 518060, P. R. China

Supporting Information

ABSTRACT: Photothermal therapy (PTT) based on two-dimensional (2D) nanomaterials has shown significant potential in cancer treatment. However, developing 2D nanomaterial-based theranostic agents with good biocompatibility and high therapeutic efficiency remains a key challenge. Bulk titanium (Ti) has been widely used as biomedical materials for their reputable biocompatibility, whereas nanosized Ti with a biological function remains unexplored. In this work, the 2D Ti nanosheets (NSs) are successfully exfoliated from nonlayer bulk Ti and utilized as an efficient theranostic nanoplatform for dual-modal computed tomography/photoacoustic (CT/PA) imaging-navigated PTT. Besides the excellent biocompatibility obtained by TiNSs as expected, they are found to show strong absorption ability with an extinction coefficient of 20.8 L g^{-1} cm^{-1} and high photothermal conversion ability with an efficiency of 61.5% owing to localized surface plasmon resonances, which exceeds most of other well-known photothermal agents, making it quite promising for PTT against cancer. Furthermore, the metallic property and light-heat-acoustic transformation endow 2D Ti with the strong CT/PA imaging signal and efficient cancer therapy, simultaneously. This work highlights the enormous potential of nanosized Ti in both the diagnosis and treatment of cancer. As a paradigm, this study also paves a new avenue for the elemental transition-metal-based cancer theranostics.

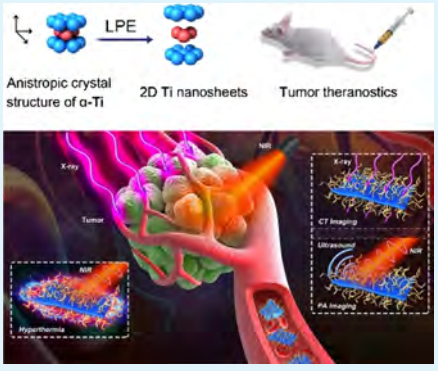

KEYWORDS: *titanium nanosheet, photothermal therapy, photoacoustic imaging, liquid-phase exfoliation, theranostic agent*

1. INTRODUCTION

Biomedical materials cover a wide scope and must exhibit a special property for one exact bio-application. The prerequisite for all biomedical materials, however, is the biocompatibility. Titanium (Ti) was first introduced in dentistry and surgeries in the 1940s to 1950s. Nowadays, Ti and its alloys are among the most attractive and important biomaterials.[1,2] They are normally applied as implant devices to take the place of the disabled hard tissues, including artificial hip joints, knee joints, bone plates, cardiac valve prostheses, artificial hearts, and dentistry devices.[3,4] The wide use of Ti in biomedicine is mainly due to its biocompatibility. It is nontoxic and won't be rejected by the body nor induce immune response after implantation. The main reason of Ti for its biocompatibility is some unique physical properties, including high resistance to corrosion,[3,5] low electronic conductivity, stable thermodynamic state at physiological environment, and low ion-production potential in water-based dispersions.[2]

In recent years, Ti-based composite nanomaterials are emerging as novel therapeutic agents against cancers. Titanium

Received: March 16, 2019
Accepted: May 30, 2019
Published: May 30, 2019

Downloaded via UNIV FRANKFURT on July 24, 2019 at 14:09:49 (UTC).
See https://pubs.acs.org/sharingguidelines for options on how to legitimately share published articles.

© 2019 American Chemical Society

DOI: 10.1021/acsami.9b04628
ACS Appl. Mater. Interfaces 2019, 11, 22129−22140

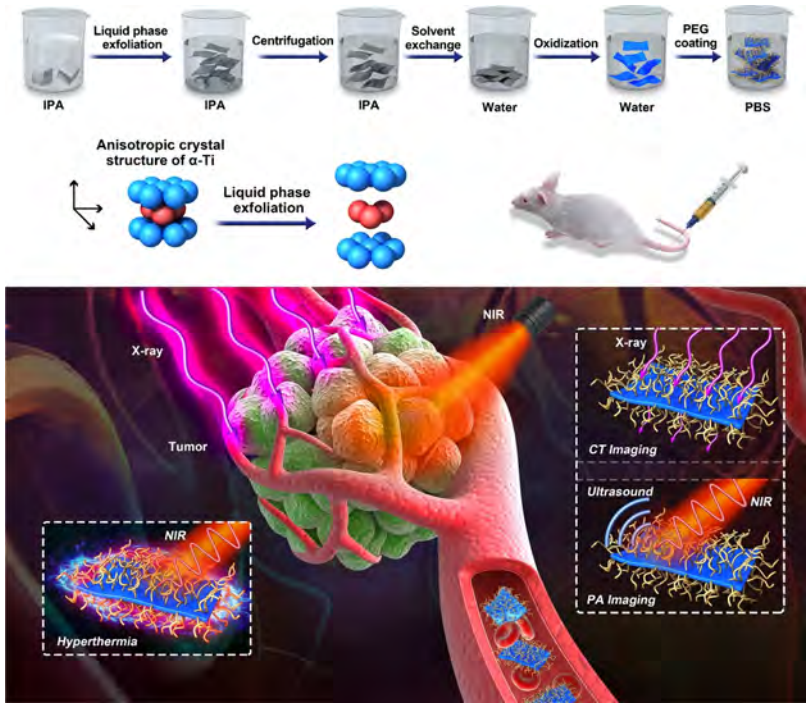

Figure 1. Schematic representation of the exfoliation and cancer theranostic applications of TiNSs.

carbide (Ti_3C_2) composite is one kind of MXene, which is an emerging class of two-dimensional (2D) early transition-metal carbides. Ti_3C_2 MXene was reported to be an effective 2D photothermal material for photothermal evaporation system.[6] Given the high photothermal efficiency of Ti_3C_2 MXene, it was also employed for photothermal therapy (PTT) with efficient tumor ablating ability[7−9] and synergistic PTT/photodynamic/chemo therapy.[10] Titanium nitride (TiN) was shown to be a plasmonic material in both visible and near-infrared wavelengths, and its performance is comparable to that of gold nanoparticles.[11] Recently, plasmonic TiN was demonstrated to be a theranostic agent for photoacoustic (PA) imaging and PTT.[12] Titanium dioxide (TiO_2) has a wide band gap, and it can efficiently absorb UV light and produce oxidative radicals.[13] After doping with nitrogen, the absorption of visible light was improved, resulting in larger radical production, making it promising for in vivo PDT of cancer.[14,15] In addition, 2D TiS_2 nanosheets (NSs) were fabricated by a bottom-up method, and the prepared TiS_2 NS can serve as a PA agent for in vivo imaging and photothermal agent.[16] As a new 2D-metal oxide/sulfide hybrid nanostructure, ultrathin $Ti_xTa_{1-x}S_yO_z$ NS was reported to exhibit a high absorption and conversion ability with the extinction coefficient up to 54.1 L g^{-1} cm^{-1} and the photothermal conversion efficiency (PTCE) of 39.2% at 808 nm.[17] Recently, magnetic Ti_3C_2 MXene nanocomposite was constructed for highly efficient cancer theranostics.[18] All these reports prove that the Ti-based composites could be an efficient photothermal and imaging agent owing to their common localized surface plasmon resonances (LSPR).

Plasmonic materials have been extensively explored as photosensitizers for PTT in NIR region over the past decade.[19−21] Compared to conventional photosensitizers, plasmonic materials not only possess stronger NIR light absorption, owing to LSPR, but also exhibit higher photostability.[21] Noble metals, such as Au, Pd, and Pt, are typical plasmonic materials and have been extensively investigated as photothermal agents.[22−28] Besides the photothermal effect, they are also attractive for other biomedical uses, such as drug delivery,[29] sensing,[30] and imaging.[31,32] However, the early transition metals with high potential for efficient photothermal conversion owing to their LSPR effect are yet to be explored.

Although liquid-phase exfoliation (LPE) has been widely used for fabrication of 2D nanomaterials such as graphene, black phosphorus, Ti_3C_2 MXene, and MoS_2, most of them are layered materials.[33−39] The nonlayered 2D materials with anisotropic bonding characteristics can be exfoliated into 2D form by the LPE method, such as ZnSe[40] and $CoSe_2$.[41] Recently, we successfully fabricated 2D selenium NSs and tellurium NSs, which are nonlayer materials with intrinsic anisotropy.[42,43] The successful fabrication intrigues us to explore the possibility of fabricating the 2D materials from other nonlayer materials with mechanical anisotropy by the LPE technique. Compared to other fabrication methods, LPE can be conducted under ambient conditions and is easy for a quantity production. Further, the resultant 2D nanomaterials have higher specific surface area, which is potential for higher drug loading capacity and thus better treatment effect for diseases such as cancers when compared to quantum dots (QDs) or 3D nanomaterials.

In this contribution, based on the widely used biocompatible material of Ti, we report the fabrication and theranostic use of a novel type of 2D nanomaterials, the TiNSs (Figure 1). It is interesting to find that nonlayer bulk Ti can be processed to give a 2D form (TiNSs) using LPE. TiNSs showed strong NIR light absorbance and efficient photothermal conversion, as evaluated by both extinction coefficient and PTCE. Moreover, the as-prepared TiNSs can also serve as contrast agents for dual-modal PA and computed tomography (CT) imaging of tumor. This work proposes the novel fabrication method for 2D TiNSs for the first time and investigates its biophotonic potential for tumor imaging and imaging-guided cancer therapy.

DOI: 10.1021/acsami.9b04628
ACS Appl. Mater. Interfaces 2019, 11, 22129−22140

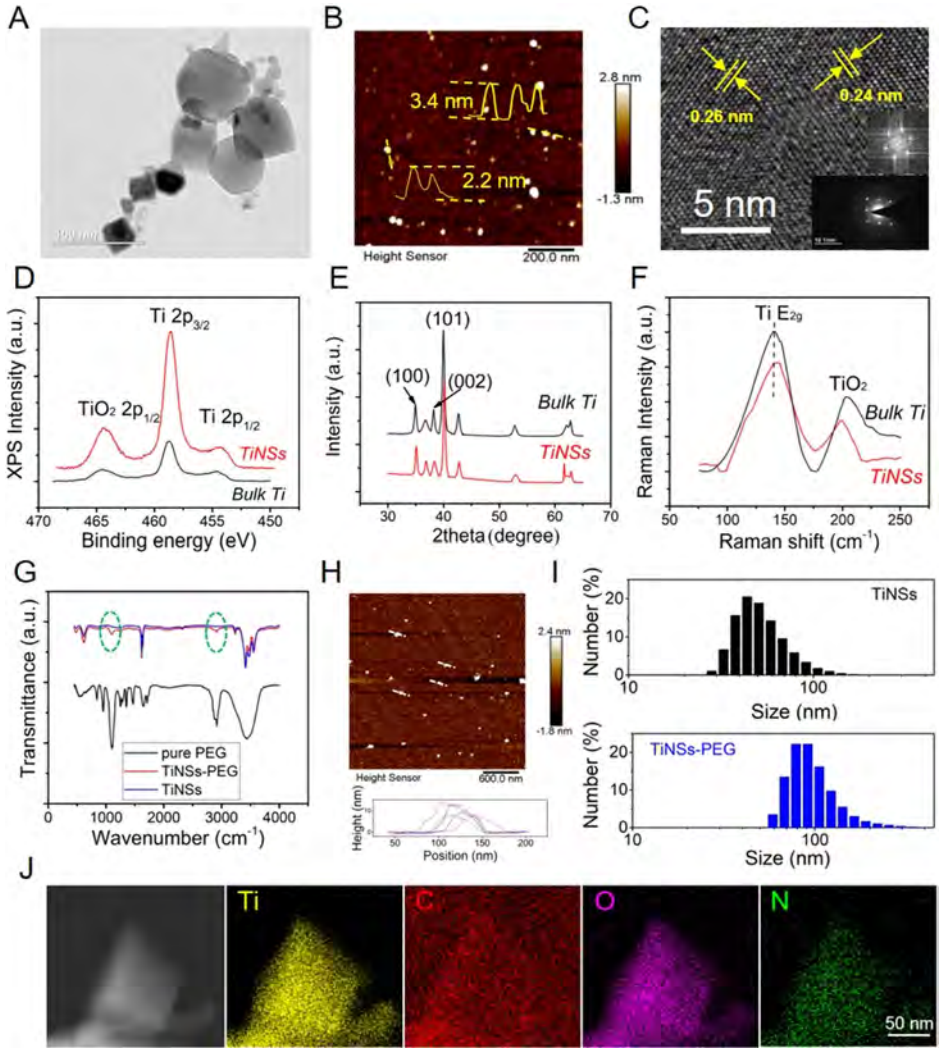

Figure 2. Characterizations of exfoliated TiNSs and TiNSs-PEG. Materials were characterized in various techniques. (A) TEM and (B) AFM image of TiNSs and Ti QDs. (C) Crystal lattice observed by high-resolution TEM and SAED of TiNSs. (D–F) XPS, XRD, and Raman spectra of bulk Ti and TiNSs. (G) FTIR spectra of pure PEG, TiNSs, and TiNSs-PEG. (H) AFM image of TiNSs-PEG. (I) Size distribution of TiNSs and TiNSs-PEG characterized by DLS. (J) STEM energy-dispersive system mapping of TiNSs-PEG.

2. RESULTS AND DISCUSSION

2.1. Fabrication and Characterization. Bulk Ti is a nonlayered metal material with a *hcp* crystal structure, which presents mechanical anisotropy. Therefore, it can be theoretically exfoliated by LPE. By using a LPE method depicted in Figure 1, as expected, morphology characterizations showed that typical 2D TiNSs were obtained (Figure 2). As for other 2D layered materials, isopropyl alcohol (IPA) was chosen as the solvent for this exfoliation. Compared with other liquid choices such as *N*-methyl-2-pyrrolidone,[44] this solvent can be easily evaporated to ensure that the surface of the obtained TiNSs is free of impurities for subsequent biological experiments. Moreover, the exfoliation efficacy in IPA is compared with that in water (Figure S1a), and IPA shows a higher efficiency shown by the enhanced absorbance for IPA-exfoliated TINSs. The exfoliation process is shown by the gradually enhanced absorbance as the exfoliation time increases (Figure S1b).

To obtain 2D TiNSs with the appropriate dimensions, dispersions of TiNSs were subjected to different degrees of centrifugal force and then characterized by typical techniques, including atomic force microscopy (AFM) and transmission electron microscopy (TEM). Different sized TiNSs observed for different centrifugal forces show different absorption abilities (Figure S2). The TEM image for the centrifugal force of 2000*g* (Figure 1A) shows the morphology of typical TiNSs with lateral dimension of less than ∼50 nm. Additionally, some Ti QDs can also be observed. The AFM characterization (Figure 2B) shows the ultrathin TiNSs with thickness of less than 5 nm. Clear lattice stripes with an interatomic distance of 0.24 and 0.26 nm are observed (Figure 2C). The selected-area electron-diffraction (SAED) pattern suggests the typical crystalline features of α-Ti (inset of Figure 2C).[45] Fast Fourier Transformation of the lattice stripes also shows the expected crystallographic lattice reflections of the TiNSs (inset of Figure 2C).

The chemical component and crystal phase of bulk Ti and TiNSs were compared through X-ray photoelectron spectroscopy (XPS) techniques. In Figure 2D, there are two XPS peaks locating at 458.58 and 454.33 eV, which come from the binding energy of the Ti $2p_{3/2}$ and Ti $2p_{1/2}$ orbitals, respectively, for both bulk Ti and TiNSs.[46,47] The XPS peak at 464.33 eV indicates the presence of TiO_2.[48] X-ray diffraction

DOI: 10.1021/acsami.9b04628
ACS Appl. Mater. Interfaces 2019, 11, 22129−22140

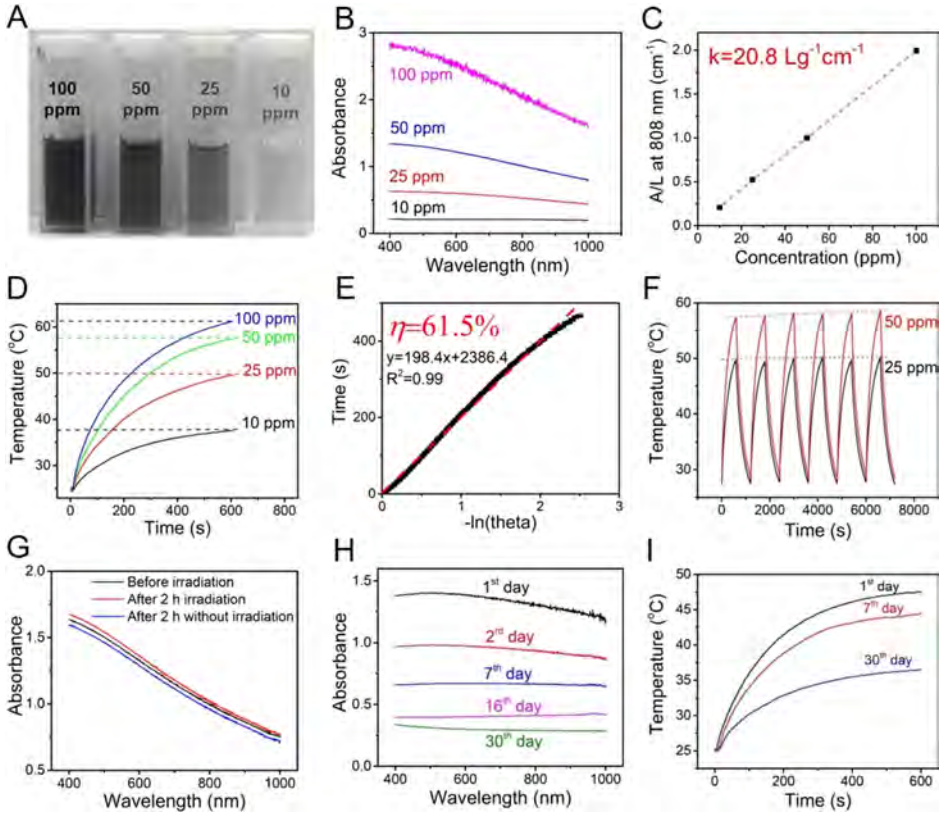

Figure 3. Light absorbance and photothermal performance of TiNSs. (A) Dispersion of TiNSs in water for different concentrations. (B) Absorption spectra of TiNSs. (C) Photothermal temperature increase of water dispersion of TiNSs. (D) Absorbance normalized by the length of light path (A/L) at 808 nm. (E) Linear fitting relationship between $-\ln\theta$ and cooling time in one photothermal cycle, to determine the PTCE. (F) Photothermal stability for several photothermal cycles. The stable photothermal performance of TiNSs was clearly observed. (G) Laser stability of TiNSs over 2 h shown by absorbance. (H,I) Temporal stability of absorbance and photothermal temperature over 30 days.

(XRD) was further characterized. The XRD pattern of exfoliated TiNSs exhibits typical Ti crystal diffraction peaks as bulk Ti (Figure 2E).[47,49] In Figure 2F, the bulk Ti and TiNSs exhibited similar Raman peaks. A sharp peak at 140.5 cm^{-1} was observed for bulk Ti, which is assigned to the zone-center E_{2g} mode of *hcp* titanium.[50] For exfoliated TiNSs, a peak at 143.8 cm^{-1} indicates a Raman shift for the ultrathin TiNSs. The peaks at ~200 cm^{-1} for both bulk Ti and exfoliated TiNSs arise as a result of TiO_2.[51]

These characterizations confirmed the dimensions, compositions, and crystal features of the exfoliated Ti nanomaterials, demonstrating the successful fabrication of 2D TiNSs. Therefore, the LPE method can be used to exfoliate nonlayered metal materials with anisotropic crystal structures in three dimensions besides layered materials with van der Waals' interactions. This widely expands the scope of the LPE method and means that more nonlayered 2D transition metal can be explored.

After being illuminated with UV light, the hydrophilic TiO_2 can be produced in the surface of TiNSs. Furthermore, the stability of TiNSs in the physiological medium can be improved by surface coating with polyethylene glycol (PEG). PEG was chosen in light of its biocompatibility and approval for medical use by the FDA. The success of this coating was characterized through scanning TEM (STEM) mapping and Fourier transform infrared spectroscopy (FTIR). For the TiNSs, the intense band at ~3400 cm^{-1} was reported to be resulted from the OH stretching. The composition of TiO_2 in the surface of TiNSs is also confirmed in the XPS and Raman measurements (Figure 2D,F). Thus, the OH group was produced by TiO_2 and made the surface of TiNSs hydrophilic.[52,53] Compared with the spectrum of TiNSs, two additional FTIR peaks emerged at ~1100 and ~2900 cm^{-1} for the PEGylated TiNSs (TiNSs-PEG). Comparison with the pure PEG spectrum (Figure 2G) showed that these two peaks can be assigned to PEG coating. The absorption band at ~2900 cm^{-1} comes from the C−H vibration, and that at ~1100 cm^{-1} is assigned to C−O stretching in the PEG unit, indicating the successful PEGylation of TiNSs. The thickness of TiNSs-PEG from the AFM image is ~10 nm (Figure 2H), which is slightly thicker than TiNSs (Figure 2B). The size range of TiNSs-PEG shifts to a larger value compared to TiNSs, as demonstrated by dynamic light scattering (DLS) characterization (Figure 2I). Moreover, the STEM mapping showed the colocalization of Ti with other three elements, C, O and N, which derive from the surface coated PEG (Figure 2J). The dispersion stability can be enhanced by this PEG decoration (Figure S5).

2.2. Light Absorbance and Photothermal Performance. Extinction coefficient defines the capacity that materials absorb light. A high extinction coefficient is a prerequisite for effective photothermal agents. To characterize this value for TiNSs, the optical absorption at different concentrations was measured. The photograph of TiNSs dispersed in water at concentrations of 10, 25, 50, and 100 ppm is shown in Figure 3A. The concentration (C) was measured using inductively coupled plasma atomic emission spectroscopy (ICP−AES). The 100 ppm dispersion was completely opaque because of the

DOI: 10.1021/acsami.9b04628
ACS Appl. Mater. Interfaces 2019, 11, 22129−22140

strong absorption of TiNSs. The optical absorption spectra of TiNSs at different concentrations (Figure 3B) shows a broad and strong absorption band covering from UV to NIR regions, same as those of other nonmetallic layered 2D materials, such as GO,[54] MoS_2,[55] WS_2,[56] and BP.[57] Strong absorption in the NIR region is necessary to take advantage of the NIR transparent window (750−1000 nm) of biological tissue for PTT.[58] The ratio of normalized absorbance (A) with the light path length (L) in the measurement cuvette (A/L) at 808 nm was determined at different concentrations (Figure 3C). Then, the extinction coefficient (k) is then calculated to be 20.8 L g^{-1} cm^{-1} at 808 nm, which is 5.3 times greater than that of AuNRs (3.9 L g^{-1} cm^{-1}),[57] on the basis of the Lambert−Beer law ($A/L = kC$). The TiNSs is also superior to other reported 2D materials in comparing with their extinction coefficient [GO NSs (3.6 L g^{-1} cm^{-1})[54] and BPQDs (14.8 L g^{-1} cm^{-1}).[57] For the larger-sized TiNSs (100−200 nm), the absorption becomes weaker as shown by the relatively small extinction coefficient (16.2 L g^{-1} cm^{-1}) (Figure S3).

Besides the absorption ability, the PTCE (η) is also the key parameter for characterizing photothermal performance. To evaluate the PTCE, the TiNSs with different concentrations of TiNSs in water were irradiated by an 808 nm laser (1.0 W cm^{-2}), which obeys the principle of that maximum permissible exposure for skin is limited to be 1.0 W cm^{-2} (American National Standard for Safe Use of Lasers, ANSI Z136.1-2007).[59,60] It is observed that even at a low concentration of 50 ppm, the temperature can increase from room temperature to 58.5 °C after 10 min irradiation (Figure 3D).

According to Roper's report,[61] the energy equilibrium for photothermal system is

$$mC_p \frac{dT}{dt} = Q_{TiNSs} + Q_s - Q_{loss} \quad (1)$$

where m, C_p, and T are the mass, heat capacity, and temperature of the solvent, respectively, Q_{TiNSs} is the laser energy input of TiNSs, Q_s is the dissipated energy by the solvent, and Q_{loss} is conductive heat transfer from the photothermal system to ambient.

The heat source term induced by laser, Q_{TiNSs}, represents the heat caused by electron−phonon relaxation of the localized plasmon at the surface of TiNSs

$$Q_{TiNSs} = I(1 - 10^{-A_{808}})\eta \quad (2)$$

I is laser power density, A_{808} is the light absorbance of the TiNSs at 808 nm, and η is the PTCE.

The heat loss term Q_{loss} is linear to the temperature of the photothermal system

$$Q_{loss} = hA(T - T_{surr}) \quad (3)$$

h is heat transfer coefficient, A is the heat transfer area, and T_{surr} is the ambient temperature.

The temperature of the photothermal system increases upon laser irradiation. The heat loss (Q_{loss}) also increases accompanying with the rise of temperature shown by eq 3. Finally, the temperature of photothermal system reaches an equilibrium value when the heat loss equates to the produced heat

$$Q_{TiNSs} + Q_S = Q_{loss\text{-}equ} = hA(T_{equ} - T_{surr}) \quad (4)$$

$Q_{loss\text{-}equ}$ represents the heat transfer off the system when the equilibrium temperature (T_{equ}) is obtained. By substituting eq 2 into eq 4, the PTCE (η) can be obtained

$$\eta = \frac{hA(T_{equ} - T_{surr}) - Q_s}{I(1 - 10^{A_{808}})} \quad (5)$$

To calculate hA, a driving force parameter of temperature increase, θ, is introduced

$$\theta = \frac{T - T_{surr}}{T_{equ} - T_{surr}} \quad (6)$$

and the heat transfer constant of photothermal system is

$$\tau_s = \frac{mc}{hA} \quad (7)$$

Substituting 6 and 7 into 2 and obtaining

$$\frac{d\theta}{dt} = \frac{1}{\tau_s}\left(\frac{Q_{TiNSs} + Q_s}{hA(T_{equ} - T_{surr})} - \theta\right) \quad (8)$$

when the laser is off, the TiNSs solvent cools down and $Q_{TiNSs} + Q_{dis} = 0$. The eq 8 can be reduced to

$$dt = -\tau_s \frac{d\theta}{\theta} \quad (9)$$

After integrating, the expression becomes

$$t = -\tau_s \ln \theta \quad (10)$$

In the cooling period, the heat transfer constant was measured and then calculated to be τ_s = 166.55 s (Figure 3E). The mass (m) of the solvent is 1 g, and the heat capacity (C_p) is 4.2 $J \cdot g^{-1}$. Then, hA can be determined according to eq 7. Substituting hA into eq 5, the PTCE (η) of TiNSs was calculated to be as high as 61.5%, which indicates that the TiNSs can efficiently produce heat through light energy conversion. The determined value was significantly larger than other important photothermal agents, including Au nanoparticles (21%),[62,63] MoS_2 (24.4%),[64] BPQDs (28.4%),[57] recently reported Ti_3C_2 MXene (30.6%),[8] BP-analogue SnS (39.3%),[65] and antimonene QDs (AMQDs, 45.5%).[66]

In addition to the extinction coefficient and PTCE, the photothermal stability is an important property for PTT. Figure 3F shows six photothermal cycles at concentrations of 25 and 50 ppm. In one photothermal cycle, the sample is irradiated intermittently by laser in each 10 min, and the temperature first increases to a saturation level and then drops down to room temperature in natural cooling process (Figure 3F). For the 25 ppm concentration, the maximum temperature during the six cycles remains consistent, illustrating that the TiNSs did not appreciably deteriorate during the 2 h photothermal process. However, for the 50 ppm sample, it was observed unexpectedly that the peak temperature increased as the photothermal cycle increased, as shown by the dotted line. We speculate that this is because water evaporation results in increasing concentration of TiNSs. This speculation is further supported by the increased absorbance after 2 h irradiation (Figure 3G). However, it was unexpectedly found that there was a slight decrease in the absorbance after 2 h of storage in water, indicating the degradability of TiNSs in water. The degradability of TiNSs was further demonstrated. As shown in Figure 3H,I it was found that both the absorbance and photothermal temperature change decreased significantly

DOI: 10.1021/acsami.9b04628
ACS Appl. Mater. Interfaces 2019, 11, 22129−22140

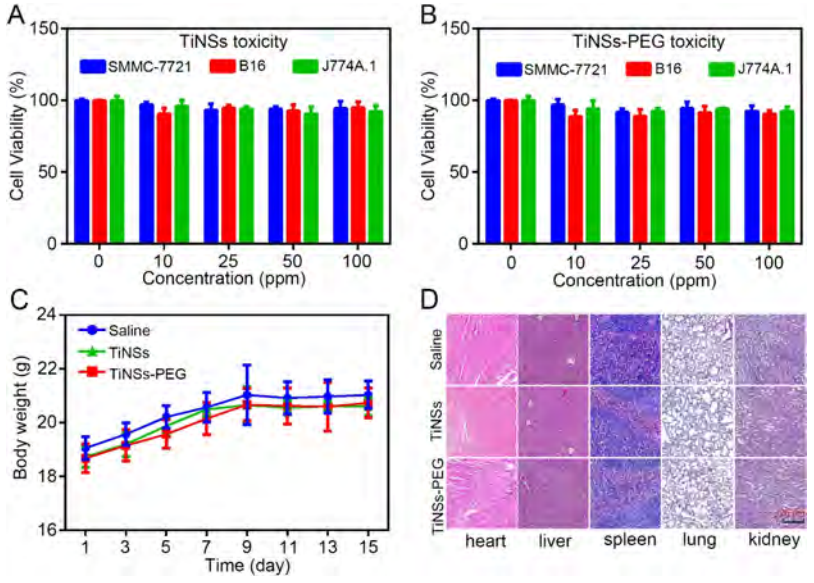

Figure 4. Toxicity assays. In vitro cytotoxicity of (A) TiNSs and (B) TiNSs-PEG was assessed using SMMC-7721, B16, and J774A.1 cells. Cells were incubated with TiNS dispersions in the concentrations of 0, 10, 25, 50, and 100 ppm. (C,D) In vivo toxicity. (C) Body weight of mice measured at the indicated time points and (D) organ conditions assessed by H&E staining at day 15 post intravenous (iv) injection of saline, TiNSs, or TiNSs-PEG.

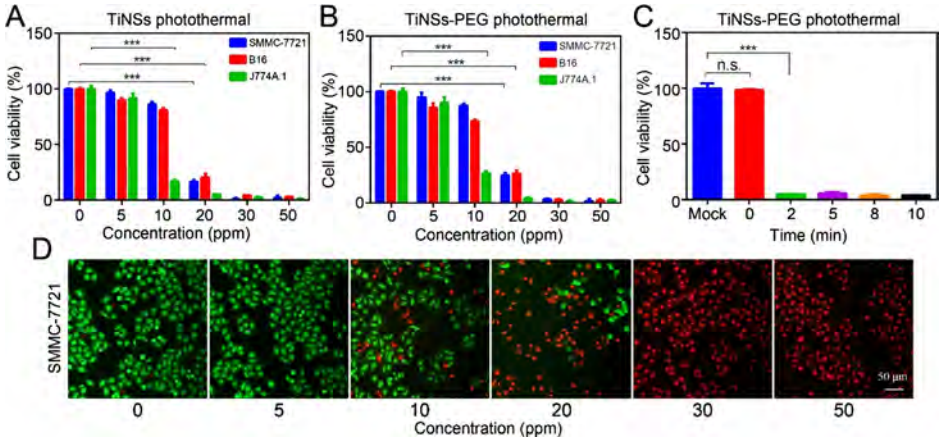

Figure 5. In vitro photothermal experiments. The photothermal killing effectiveness of (A) TiNSs and (B) TiNSs-PEG on SMMC-7721, B16, and J774A.1 cells for different concentrations under the same NIR irradiation conditions (1.0 W cm^{-2}, 5 min). (C) Photothermal cell killing effect of TiNSs-PEG (50 ppm) for different irradiation time courses. (D) Fluorescent image of photothermal effect on SMMC-7721 cells postirradiation, as assessed by calcein AM/PI staining 6 h after irradiation. $n = 3$ biological replicates, n.s. stands for non-significant, $^{***}p < 0.001$, Student's t-tests.

after 30 days. Quantitatively, absorbance measurements showed that 77% of the TiNSs was degraded, but the photothermal temperature only degraded by 47%. The degradation product was TiO_2, as demonstrated by the XPS characterization in Figure 2, the degradation product was TiO_2. TiO_2 may have a significant impact on the decrease in absorbance but led to only a minor decrease of photothermal temperature because it can also contribute to the photothermal temperature rise.[67−69] Moreover, the degradability of TiNSs-PEG in PBS was also proved (Figure S4).

Consequently, the as-prepared 2D TiNSs showed high extinction coefficient (20.8 L g^{-1} cm^{-1}), high PTCE (61.5%), good photostability, and degradability. These properties make TiNSs quite valuable and promising in many biomedical applications, such as diagnosis and treatment against cancer that is further explored in this work.

2.3. Toxicity Assays. Ti metal is well known for its excellent biocompatibility; however, the cytotoxicity of the newly fabricated TiNSs had to be evaluated to support their further biomedical application. The potential cytotoxicity of both TiNSs and TiNSs-PEG was evaluated in this work. Tumor microenvironments consist of various kinds of cells, including tumor infiltrating immune cells. To model the tumor microenvironment, both cancer and normal cells were incubated with the TiNSs, including SMMC-7721 (hepatocellular carcinoma), B16 (melanoma), and J774A.1 (macrophage). As shown in Figure 4A,B, both TiNS- and TiNSs-PEG-treated cells exhibited minimal inhibition of proliferation in CCK8 assays posttreatment even at high concentration (100 ppm). Moreover, the targeting effect of TiNSs-PEG to cancer cells further reduces the potential toxicity to normal cells (Figure S6).

DOI: 10.1021/acsami.9b04628
ACS Appl. Mater. Interfaces 2019, 11, 22129−22140

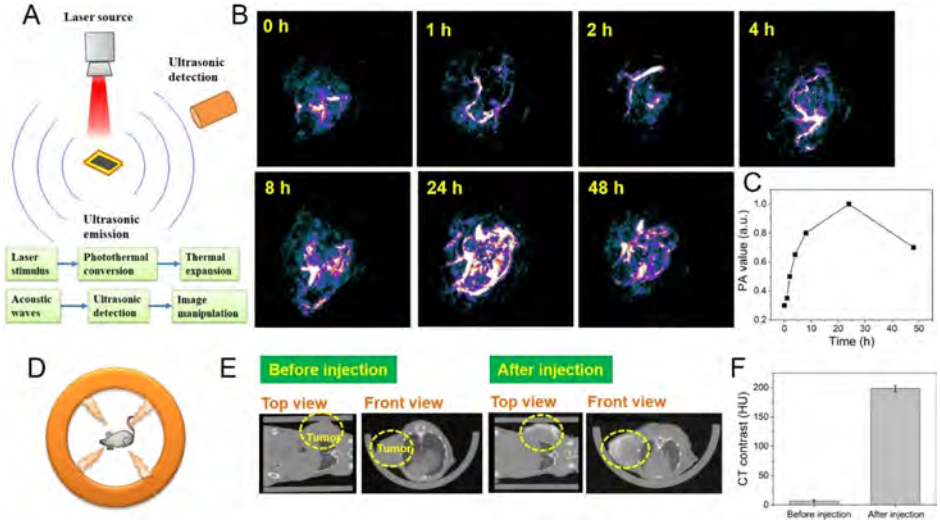

Figure 6. Multimodal imaging of TiNSs-PEG. (A) Schematic illustration of PA imaging. PA imaging is an emerging biomedical imaging technique based on the light-heat-acoustic signal conversion with the notably advantage of enhanced imaging depth in contrast to traditional optical imaging methods. (B) PA images and (C) PA signal value of tumor site at different time points postinjection (5 mg kg^{-1}). (D) Schematic illustration of CT imaging. (E) In vivo CT contrast images and (F) CT signal value before (right) and after (left) intravenous injection (5 mg kg^{-1}).

The in vivo toxicity of TiNSs was further investigated. Figure 4C shows that the body weights of the mice treated with TiNSs or TiNSs-PEG showed no difference from those injected with saline, suggesting that the TiNSs did not intrinsically affect the overall condition of the mice. In addition, the pathological changes of the major organs were sliced for hematoxylin and eosin (H&E) staining, and no significant histological abnormalities were found (Figure 4D). The degradation of TiNSs in main organs was also proved (Figure S7). Moreover, the hematological parameters of tumor-bearing mice with different treatments were determined. As shown in Figure S9, no significant differences were observed between different treatments, further demonstrating the nontoxic TiNSs.

Consequently, all of the results demonstrate that TiNSs were nontoxic both in vitro and in vivo. More importantly, the excellent biocompatibility of TiNSs is evidenced to be the intrinsic attribute of Ti, rather than through biocompatible surface modification, supporting further in vivo PTT.

2.4. In Vitro Photothermal Experiments. Based on the high photothermal performance and biocompatibility of TiNSs, high tumor cell killing efficiency of TiNSs was anticipated. As shown in Figure 5A,B, both TiNSs and TiNSs-PEG showed a clear photothermal killing effect as concentration increased. SMMC-7721 and B16 cells (75%) were killed at 20 ppm, and nearly all of the cells can be killed at a low concentration of 30 ppm. J774A.1 cells were particularly vulnerable, with only ~25% of the cells surviving after the photothermal killing process at 10 ppm. The enhanced efficiency is probably because J774A.1 cells can intake more TiNSs than cancer cells because of phagocytosis, resulting in higher photothermal efficiency.

Additionally, we investigated the laser irradiation time required for 100% cell killing efficacy at 50 ppm. It was found that a short time of 2 min is enough to kill the vast majority of the cells (Figure 5C). We speculated that the efficient cell killing could result from the sharp increase in temperature induced by NIR irradiation. Graphic illustrations of the photothermal killing effect for different concentrations of TiNSs are presented in Figure 5D, which is consistent with results of CCK8 assays. The high photothermal killing effect of TiNSs toward tumor-retained cells was thus demonstrated.

2.5. Dual-Modal Imaging Performance of TiNSs-PEG. Given the strong NIR-absorbance and high PTCE of TiNSs in the NIR region, an emerging imaging strategy, that is, PA imaging, was explored by employing TiNSs-PEG (Figure 6A). The in vitro imaging characterizations of TiNSs show an enhanced contrast for both PA and CT agents (Figure S8). The cervical-tumor-bearing mice were injected with TiNSs-PEG (5 mg kg^{-1}) in an iv way and PA signal was acquired at consecutive time points. As time increased from 0 to 24 h, the intensity of PA signal increased gradually because of the accumulation of TiNSs-PEG by means of the enhanced permeability and retention effect (Figure 6B,C). The tumor site was clearly enlightened at 24 h postinjection. Then, the PA signal decreased owing to metabolism of TiNSs-PEG. Furthermore, the TiNSs-PEG was investigated as a CT agent owing to their metallic property for attenuating X-ray (Figure 6D). The saline solution containing TiNSs-PEG (5 mg kg^{-1}) was iv injected into the cervical-tumor-bearing mice. Twenty-four hours postinjection, the CT images and CT signal value revealed evident tumor contrast (Figure 6E,F). Therefore, these observations prove that TiNSs-PEG could efficiently accumulate in the tumor and act as PA and CT agents for bioimaging of tumors.

2.6. In Vivo PTT Against Cancer. To estimate the in vivo anticancer activity, the circulation kinetics and biodistribution dynamics of TiNSs after iv injection were monitored. The quantity of TiNSs-PEG circulated in bloodstream was measured at different points in time, and the half-time of the blood circulation was determined to be 1.8 h (Figure 7A). The biodistribution of TiNSs-PEG in tumor and major organs was investigated at a time point of 24 h after iv injection. The intratumoral accumulation efficiency was quantified to be 3.5% ID/g by using ICP−mass spectrometry (ICP−MS) technology (Figure 7B). The relative long blood circulation time and efficient tumor site accumulation of TiNSs are beneficial for high-efficient in vivo PTT.

Furthermore, the in vivo PTT investigations were conducted through iv injection of TiNSs-PEG. To study the PTT efficacy,

DOI: 10.1021/acsami.9b04628
ACS Appl. Mater. Interfaces 2019, 11, 22129−22140

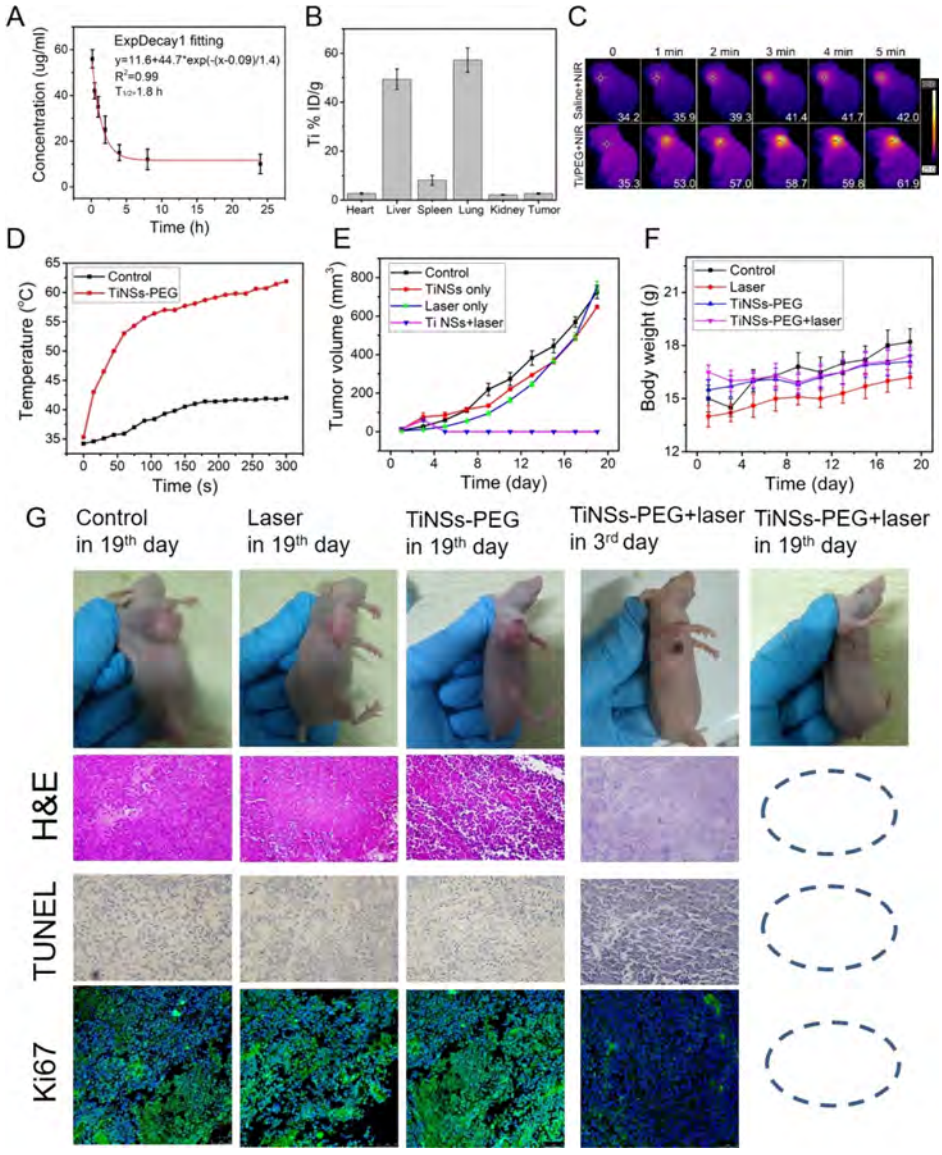

Figure 7. In vivo photothermal tumor therapy. (A) Blood circulation period of TiNSs-PEG after iv injection (n = 3). (B) Biodistribution of Ti (% ID/g of organs) in major tissues and tumor. (C) Infrared images of tumor-bearing mice in G2 (laser only) and G4 (TiNSs-PEG + laser) upon irradiation. (D) Time-dependent temperature changes at the tumor site. (E) Growth changes of tumor volume of the four groups. (F) Body weight change of the four groups. (G) Photographs of hepatocellular carcinoma tumor-bearing mice for four groups. To uncover the mechanism of in vivo PTT of TiNSs-PEG, three straining strategies for pathological changes in tumor slice were employed for each group, including H&E, TUNEL and Antigen Ki-67 immunofluorescence staining.

hepatocellular carcinoma tumor-bearing mice models were established and subjected to different treatment: G1: control, G2: NIR laser only, G3: TiNSs-PEG only (dose of 2 mg kg^{-1}), and G4: TiNSs-PEG + NIR laser (dose of 2 mg kg^{-1}). The temperature change at the irradiation site was monitored during the NIR irradiation period. As shown in the infrared images in Figure 7C,D, the temperature of the irradiation site for the laser-only group slightly increased to 42 °C during the NIR irradiation period. However, for TiNSs-PEG, the temperature increased to 53 °C during a short irradiation time (1 min), and then the temperature increased slowly to a final 61.9 °C in the further irradiation of 5 min, which was enough to kill the tumor cell and ablate the tumor.

The tumor volumes of the mice in four groups were measured every other day (Figure 7E). For G1, G2, and G3, it was observed that the tumor grew fast during 19 days. However, tumors of G4 disappeared within 5 days after PTT, leaving black scars in the tumor sites, confirming the high-efficient treatment of TiNSs-PEG-based PTT. The weight of the treated mice was also measured during the course of the treatment (Figure 7F). We found that the different treatments had little influence on body weight, indicating that the laser, TiNSs-PEG, and PTT do not affect growth of mice. Good biosafety of TiNSs-PEG-based PTT was therefore demonstrated.

To reveal the mechanism of PTT exerted by TiNSs-PEG, the tumors of each group were isolated and subjected to three kinds of staining techniques, including H&E, Ki-67 antibody, and TdT-mediated dUTP nick-end Labeling (TUNEL) staining. The tumor ablation effect was observed from H&E-staining micrographs of G4 (Figure 7G) but not in the other three groups. Similar to the H&E-staining results, TUNEL

DOI: 10.1021/acsami.9b04628
ACS Appl. Mater. Interfaces 2019, 11, 22129−22140

staining also illustrated much higher cell necrosis in tumor tissues in G4 group than other three groups. Furthermore, to evaluate the suppression effect to cancer cell proliferation, Ki-67 antibody staining was performed. The G4 group in the 3rd day exhibited a strong inhibition effect on proliferation of cancer cell, while the other three groups did not. Taken together, these observations demonstrated that the high in vivo photothermal ablation effect of TiNSs-PEG resulted from comprehensive mechanisms, such as rapid destruction of tumor, induction of necrosis, and suppression of proliferation of tumor cells. In aggregates, the TiNSs-PEG-based PTT was efficient and minimally invasive and thus was a promising alternative to traditional therapy methods.

3. CONCLUSION

In this work, nonlayered metallic Ti was fabricated into 2D NSs using a LPE strategy, with an average thickness of ~3 nm and lateral size of less than 50 nm. Ultrathin TiNSs exhibited a high absorption ability with an extinction coefficient of 20.8 L g^{-1} cm^{-1}. They also showed a high PTCE of 61.5% under NIR irradiation (808 nm laser), owing to the LSPR resulting from the metallic nature of TiNSs. This photothermal conversion ability significantly exceeds those of classic photothermal agents such as Au and newly emerged 2D materials, such as MoS_2, black phosphorus, and Ti_3C_2 MXene. The TiNSs also degraded in a relatively short time (77% degradation over 30 days in water at ~30 °C). The degradability may help avoid long-term damage to the human reticular system and further improve its clinical potential. In addition to high photothermal performance, dual-modal contrast-enhanced PA and CT imaging in vivo were achieved because of the strong NIR light absorbance and high X-ray response ability of TiNSs, giving it a diagnostic function for tumor.

All in all, taking together the biocompatibility, biodegradability, high PTCE and enhanced contrast as PA and CT agents, TiNSs combine the diagnostic and therapeutic functions against cancers, making it a promising theranostic agent for clinical use.

4. EXPERIMENTAL SECTION

4.1. Ti Nanosheets Fabrication. The ultrathin TiNSs were prepared from bulk Ti using LPE. Ti powder (500 mg) was mixed with IPA (100 mL). The suspension was then subjected to probe sonication for 10 h at the power of 240 W. Subsequently, the Ti dispersion underwent bath sonication at a power of 360 W for 10 h. The resulting dispersions were centrifuged at 2000*g* for 30 min to remove the unexfoliated component. The supernatant containing the TiNSs was decanted gently and then centrifuged for a further 30 min at 12 000*g*. The precipitate was dried in a vacuum drying oven. The TiNSs-PEG were further prepared. DSPE-PEG (1 mg) was dispersed in 1 mL of water. TiNSs dispersion (5 mL) in water with a concentration of 100 ppm was involved sonication for 30 min and then mixed with PEG solution. The mixture underwent bath sonication for several min and was stirred for 3 h. Then, to remove the excess PEG molecules, the resulting mixture was ultrafiltered in Amicon tubes (MWCO 100 kDa; Millipore) at 1000*g* until all water was filtered out and was washed twice using the same method. The pure TiNSs-PEG was resuspended in ultrapure water or culture media for further use.

4.2. Characterization. The morphology of TiNSs was observed by AFM and TEM. The crystalline structure and elemental composition were measured with HRTEM images, SAED, XRD, XPS, and ICP–MS. The absorbance and verification of PEG coating on TiNSs were acquired by using a Cary 60 spectrometer and measuring the FTIR spectrum, respectively. PTCE and biodegradability of TiNSs dispersion were also measured.

4.3. Cell Culture. Mouse melanoma cells (B16) and mouse macrophage cells (J774A.1) were incubated in the Dulbecco's modified Eagle medium (DMEM) with high concentrated glucose (Hyclone). Human hepatocellular carcinoma cells (SMMC-7721) were incubated in a mixture of Ham's F-12 medium (Hyclone) and DMEM with a mixture ratio of 1:1.Pen/Strep (Gibco) (1%) and fetal bovine serum (Gibco) (10%) were used to supplement the culture medium and the culture condition is 5% CO_2 at 37 °C.

4.4. In Vitro Experiments. Cells seeded in 96-well plates were treated with TiNSs, TiNSs-PEG, or left untreated (Mock). For in vitro cytotoxicity assays, cells were directly subjected to cell-counting kit (CCK8) tests (Beyotime Biotechnology) 24 h post TiNSs incubation. For in vitro photothermal study, cells coexisted with TiNSs for 4 h and then experienced a radiation using a 808 nm laser with a power density of 1.0 W cm^{-2} for 5 min. Finally, the cells went through the CCK8 tests following the manufacturer's instructions 24 h postirradiation. The relative cell viability was normalized to the Mock samples (concentration of TiNSs = 0 ppm) of each cell line. To show the photothermal killing effect, cells were subjected to calcein AM/PI staining (Sigma) 6 h postirradiation. The live cells and dead cells appear to be green and red color stained by calcein AM and PI, respectively. The targeting experiments in vitro toward cancer cells (SMMC-7721) and normal cells (HL-7702) were conducted.

4.5. In Vivo Toxicity. Six-week-old female Balb/c nude mice were used for toxicity assays and establishment of tumor-bearing mouse models. Mice were randomly distributed into three groups (n = 5 each group) and were intravenously injected with saline, TiNSs, and TiNSs-PEG at the first day. The dose of TiNSs or TiNSs-PEG was 5 mg kg^{-1}. To monitor the in vivo toxicity, the body weight was measured every 2 days until the 19th day. The mice were then euthanized, and the major organs of heart, liver, spleen, lung, and kidney were incised for H&E staining. Furthermore, the degradation of TiNSs in vivo was proved at different time points after iv injection.

4.6. Dual-Modal in Vivo PA and CT Imaging. For in vivo PA imaging, the cervical-tumor-holding mice were intravenously treated with 200 μL of TiNSs-PEG samples (5 mg mL^{-1}). After the treatment, the PA experiments were conducted at different times (0, 1, 2, 4, 8, 24, and 48 h). For in vivo CT imaging, 200 μL of TiNSs-PEG (5 mg mL^{-1}) was intravenously injected. The mice were set on the CT equipment to image before injection and postinjection for 24 h.

4.7. In Vivo Photothermal Tumor Therapy. The mice were randomly distributed into four groups (n = 5 for each group) for different treatments by iv injection: group 1, saline; group 2, TiNSs-PEG; group 3, saline with NIR irradiation; and group 4, TiNSs-PEG with NIR irradiation. The TiNSs-PEG was injected intravenously in a dosage of 2 mg kg^{-1}. Twenty-four hours postinjection, the mice were anaesthetized, and the tumors were irradiated by the 808 nm laser (1.0 W cm^{-2}, 5 min). The temperature of the tumor was measured using thermography. After the photothermal treatment, the tumor volumes and body weights were recorded every 2 days. The tumor size was measured using a caliper, and the volumes were calculated through the equation (volume = length × width^2/2, $V = l \times w^2/2$). At the 19th day, all of the mice were euthanized, and the organs of heart, liver, spleen, lung, and kidney were isolated for H&E staining to assess the possible damage caused by the PTT.

4.8. Haematology Tests. The normal haematology tests were conducted by measuring red blood cells, white blood cells, platelets, haemoglobin, mean corpuscular haemoglobin (MCH), MCH concentration, haematocrit, and mean corpuscular volume.

■ ASSOCIATED CONTENT

Supporting Information

The Supporting Information is available free of charge on the ACS Publications website at DOI: 10.1021/acsami.9b04628.

Fabrication and characterization methods of TiNSs; calculation of PTCE; toxicity test; cell culture and

DOI: 10.1021/acsami.9b04628
ACS Appl. Mater. Interfaces 2019, 11, 22129–22140

mouse experiments details; and dual-modal PA and CT imaging procedure and haematology test (PDF)

AUTHOR INFORMATION

Corresponding Authors

*E-mail: leoliping@aliyun.com (L.L.).
*E-mail: chenhongcs@126.com (H.C.).
*E-mail: hzhang@szu.edu.cn (H.Z.).

ORCID

Han Zhang: 0000-0002-2197-7270

Author Contributions

¶Z.X., S.C., Y.D., Y.Z., and T.F. contributed equally to this work.

Notes

The authors declare no competing financial interest.

ACKNOWLEDGMENTS

This research is partially supported by the National Natural Science Fund (grant nos. 61435010 and 61575089), Science and Technology Innovation Commission of Shenzhen (KQTD20150324162703855, JCYJ20150625103619275 and GRCK2017082111070420), and China Postdoctoral Science Foundation (grant nos 2017M612730 and 2018M640817).

REFERENCES

(1) Oliveira, W. F.; Arruda, I. R. S.; Silva, G. M. M.; Machado, G.; Coelho, L. C. B. B.; Correia, M. T. S. Functionalization of Titanium Dioxide Nanotubes with Biomolecules for Biomedical Applications. *Mater. Sci. Eng., C* **2017**, *81*, 597−606.

(2) Elias, C. N.; Lima, J. H. C.; Valiev, R.; Meyers, M. A. Biomedical Applications of Titanium and Its Alloys. *JOM* **2008**, *60*, 46−49.

(3) Wen, C. E.; Yamada, Y.; Shimojima, K.; Chino, Y.; Asahina, T.; Mabuchi, M. Processing and Mechanical Properties of Autogenous Titanium Implant Materials. *J. Mater. Sci.: Mater. Med.* **2002**, *13*, 397−401.

(4) de Avila, E. D.; Lima, B. P.; Sekiya, T.; Torii, Y.; Ogawa, T.; Shi, W.; Lux, R. Effect of UV-Photofunctionalization on Oral Bacterial Attachment and Biofilm Formation to Titanium Implant Material. *Biomaterials* **2015**, *67*, 84−92.

(5) Spriano, S.; Bronzoni, M.; Rosalbino, F.; Vernè, E. New Chemical Treatment for Bioactive Titanium Alloy with High Corrosion Resistance. *J. Mater. Sci.: Mater. Med.* **2005**, *16*, 203−211.

(6) Li, R.; Zhang, L.; Shi, L.; Wang, P. MXene Ti3C2: An Effective 2D Light-to-Heat Conversion Material. *ACS Nano* **2017**, *11*, 3752−3759.

(7) Xuan, J.; Wang, Z.; Chen, Y.; Liang, D.; Cheng, L.; Yang, X.; Liu, Z.; Ma, R.; Sasaki, T.; Geng, F. Organic-Base-Driven Intercalation and Delamination for the Production of Functionalized Titanium Carbide Nanosheets with Superior Photothermal Therapeutic Performance. *Angew. Chem., Int. Ed.* **2016**, *55*, 14569−14574.

(8) Lin, H.; Wang, X.; Yu, L.; Chen, Y.; Shi, J. Two-Dimensional Ultrathin MXene Ceramic Nanosheets for Photothermal Conversion. *Nano Lett.* **2017**, *17*, 384−391.

(9) Xing, C.; Chen, S.; Liang, X.; Liu, Q.; Qu, M.; Zou, Q.; Li, J.; Tan, H.; Liu, L.; Fan, D.; et al. Two-Dimensional MXene (Ti3C2)-Integrated Cellulose Hydrogels: Toward Smart Three-Dimensional Network Nanoplatforms Exhibiting Light-Induced Swelling and Bimodal Photothermal/Chemotherapy Anticancer Activity. *ACS Appl. Mater. Interfaces* **2018**, *10*, 27631−27643.

(10) Liu, G.; Zou, J.; Tang, Q.; Yang, X.; Zhang, Y.; Zhang, Q.; Huang, W.; Chen, P.; Shao, J.; Dong, X. Surface Modified Ti3C2 MXene Nanosheets for Tumor Targeting Photothermal/Photodynamic/Chemo Synergistic Therapy. *ACS Appl. Mater. Interfaces* **2017**, *9*, 40077−40086.

(11) Li, W.; Guler, U.; Kinsey, N.; Naik, G. V.; Boltasseva, A.; Guan, J.; Shalaev, V. M.; Kildishev, A. V. Refractory Plasmonics with Titanium Nitride: Broadband Metamaterial Absorber. *Adv. Mater.* **2014**, *26*, 7959−7965.

(12) He, W.; Ai, K.; Jiang, C.; Li, Y.; Song, X.; Lu, L. Plasmonic Titanium Nitride Nanoparticles for in Vivo Photoacoustic Tomography Imaging and Photothermal Cancer Therapy. *Biomaterials* **2017**, *132*, 37−47.

(13) Chen, X.; Mao, S. S. Titanium Dioxide Nanomaterials: Synthesis, Properties, Modifications, and Applications. *Chem. Rev.* **2007**, *107*, 2891−2959.

(14) Xiang, Q.; Yu, J.; Wang, W.; Jaroniec, M. Nitrogen Self-Doped Nanosized TiO2 Sheets with Exposed {001} Facets for Enhanced Visible-Light Photocatalytic Activity. *Chem. Commun.* **2011**, *47*, 6906−6908.

(15) Asahi, R.; Morikawa, T.; Ohwaki, T.; Aoki, K.; Taga, Y. Visible-Light Photocatalysis in Nitrogen-Doped Titanium Oxides. *Science* **2001**, *293*, 269−271.

(16) Qian, X.; Shen, S.; Liu, T.; Cheng, L.; Liu, Z. Two-Dimensional TiS2 Nanosheets for in Vivo Photoacoustic Imaging and Photothermal Cancer Therapy. *Nanoscale* **2015**, *7*, 6380−6387.

(17) Tan, C.; Zhao, L.; Yu, P.; Huang, Y.; Chen, B.; Lai, Z.; Qi, X.; Goh, M. H.; Zhang, X.; Zhang, H. Preparation of Ultrathin Two-Dimensional TixTa1-xSyOz Nanosheets as Highly Efficient Photothermal Agents. *Angew. Chem., Int. Ed.* **2017**, *56*, 7842−7846.

(18) Liu, Z.; Zhao, M.; Lin, H.; Dai, C.; Chen, Y. 2D Magnetic Titanium Carbide (MXene) for Cancer Theranostics. *J. Mater. Chem. B* **2018**, *6*, 3541−3548.

(19) He, W.; Ai, K.; Jiang, C.; Li, Y.; Song, X.; Lu, L. Plasmonic Titanium Nitride Nanoparticles for in Vivo Photoacoustic Tomography Imaging and Photothermal Cancer Therapy. *Biomaterials* **2017**, *132*, 37−47.

(20) Howes, P. D.; Rana, S.; Stevens, M. M. Plasmonic nanomaterials for biodiagnostics. *Chem. Soc. Rev.* **2014**, *43*, 3835−3853.

(21) De Aberasturi, D. J.; Serrano-Montes, A. B.; Liz-Marzán, L. M. Modern Applications of Plasmonic Nanoparticles: From Energy to Health. *Adv. Opt. Mater.* **2015**, *3*, 602−617.

(22) Huang, X.; Tang, S.; Mu, X.; Dai, Y.; Chen, G.; Zhou, Z.; Ruan, F.; Yang, Z.; Zheng, N. Freestanding Palladium Nanosheets with Plasmonic and Catalytic Properties. *Nat. Nanotechnol.* **2011**, *6*, 28−32.

(23) Aioub, M.; Panikkanvalappil, S. R.; El-Sayed, M. A. Platinum-Coated Gold Nanorods: Efficient Reactive Oxygen Scavengers That Prevent Oxidative Damage toward Healthy, Untreated Cells during Plasmonic Photothermal Therapy. *ACS Nano* **2017**, *11*, 579−586.

(24) Chen, M.; Tang, S.; Guo, Z.; Wang, X.; Mo, S.; Huang, X.; Liu, G.; Zheng, N. Core-Shell Pd@Au Nanoplates as Theranostic Agents for in-Vivo Photoacoustic Imaging, CT Imaging, and Photothermal Therapy. *Adv. Mater.* **2014**, *26*, 8210−8216.

(25) Cheng, X.; Sun, R.; Yin, L.; Chai, Z.; Shi, H.; Gao, M. Light-Triggered Assembly of Gold Nanoparticles for Photothermal Therapy and Photoacoustic Imaging of Tumors In Vivo. *Adv. Mater.* **2017**, *29*, 1604894−1604900.

(26) Li, N.; Zhao, P.; Astruc, D. Anisotropic Gold Nanoparticles: Synthesis, Properties, Applications, and Toxicity. *Angew. Chem., Int. Ed.* **2014**, *53*, 1756−1789.

(27) Amendola, V.; Pilot, R.; Frasconi, M.; Maragò, O. M.; Iatì, M. A. Surface Plasmon Resonance in Gold Nanoparticles: A Review. *J. Phys.: Condens. Matter* **2017**, *29*, 203002.

(28) Zhou, J.; Meng, L.; Lu, Q. Core@shell Nanostructures for Photothermal Conversion: Tunable Noble Metal Nanoshells on Cross-Linked Polymer Submicrospheres. *J. Mater. Chem.* **2010**, *20*, 5493−5498.

(29) Hu, F.; Zhang, Y.; Chen, G.; Li, C.; Wang, Q. Double-Walled Au nanocage/SiO_2 Nanorattles: Integrating SERS Imaging, Drug Delivery and Photothermal Therapy. *Small* **2015**, *11*, 985−993.

DOI: 10.1021/acsami.9b04628
ACS Appl. Mater. Interfaces 2019, 11, 22129−22140

(30) Wang, L.; Dou, H.; Lou, Z.; Zhang, T. Encapsuled Nanoreactors (Au@SnO2): A New Sensing Material for Chemical Sensors. *Nanoscale* **2013**, *5*, 2686−2691.
(31) Liu, X.; Zhang, X.; Zhu, M.; Lin, G.; Liu, J.; Zhou, Z.; Tian, X.; Pan, Y. PEGylated Au@Pt Nanodendrites as Novel Theranostic Agents for Computed Tomography Imaging and Photothermal/Radiation Synergistic Therapy. *ACS Appl. Mater. Interfaces* **2017**, *9*, 279−285.
(32) Li, J.; Hu, Y.; Yang, J.; Wei, P.; Sun, W.; Shen, M.; Zhang, G.; Shi, X. Hyaluronic acid-modified Fe3O4@Au core/shell nanostars for multimodal imaging and photothermal therapy of tumors. *Biomaterials* **2015**, *38*, 10−21.
(33) Qiu, M.; Ren, W. X.; Jeong, T.; Won, M.; Park, G. Y.; Sang, D. K.; Liu, L.-P.; Zhang, H.; Kim, J. S. Omnipotent Phosphorene: A next-Generation, Two-Dimensional Nanoplatform for Multidisciplinary Biomedical Applications. *Chem. Soc. Rev.* **2018**, *47*, 5588−5601.
(34) Tang, X.; Chen, H.; Ponraj, J. S.; Dhanabalan, S. C.; Xiao, Q.; Fan, D.; Zhang, H. Fluorination-Enhanced Ambient Stability and Electronic Tolerance of Black Phosphorus Quantum Dots. *Adv. Sci.* **2018**, *5*, 1800420−1800429.
(35) Tang, X.; Liang, W.; Zhao, J.; Li, Z.; Qiu, M.; Fan, T.; Luo, C. S.; Zhou, Y.; Li, Y.; Guo, Z.; et al. Fluorinated Phosphorene: Electrochemical Synthesis, Atomistic Fluorination, and Enhanced Stability. *Small* **2017**, *13*, 1702739.
(36) Wu, L.; Xie, Z.; Lu, L.; Zhao, J.; Wang, Y.; Jiang, X.; Ge, Y.; Zhang, F.; Lu, S.; Guo, Z.; et al. Few-Layer Tin Sulfide: A Promising Black-Phosphorus-Analogue 2D Material with Exceptionally Large Nonlinear Optical Response, High Stability, and Applications in All-Optical Switching and Wavelength Conversion. *Adv. Opt. Mater.* **2018**, *6*, 1700985.
(37) Huang, W.; Xie, Z.; Fan, T.; Li, J.; Wang, Y.; Wu, L.; Ma, D.; Li, Z.; Ge, Y.; Huang, Z. N.; et al. Black-Phosphorus-Analogue Tin Monosulfide: An Emerging Optoelectronic Two-Dimensional Material for High-Performance Photodetection with Improved Stability under Ambient/harsh Conditions. *J. Mater. Chem. C* **2018**, *6*, 9582−9593.
(38) Fan, T.; Zhou, Y.; Qiu, M.; Zhang, H. Black Phosphorus: A Novel Nanoplatform with Potential in the Field of Bio-Photonic Nanomedicine. *J. Innovative Opt. Health Sci.* **2018**, *11*, 1830003−1830023.
(39) Qiu, M.; Wang, D.; Liang, W.; Liu, L.; Zhang, Y.; Chen, X.; Sang, D. K.; Xing, C.; Li, Z.; Dong, B.; Xing, F.; Fan, D.; Bao, S.; Zhang, H.; Cao, Y. Novel Concept of the Smart NIR-Light-Controlled Drug Release of Black Phosphorus Nanostructure for Cancer Therapy. *Proc. Natl. Acad. Sci. U.S.A.* **2018**, *115*, 501−506.
(40) Sun, Y.; Sun, Z.; Gao, S.; Cheng, H.; Liu, Q.; Piao, J.; Yao, T.; Wu, C.; Hu, S.; Wei, S.; Xie, Y. Fabrication of Flexible and Freestanding Zinc Chalcogenide Single Layers. *Nat. Commun.* **2012**, *3*, 1057.
(41) Liu, Y.; Cheng, H.; Lyu, M.; Fan, S.; Liu, Q.; Zhang, W.; Zhi, Y.; Wang, C.; Xiao, C.; Wei, S.; Ye, B.; Xie, Y. Low Overpotential in Vacancy-Rich Ultrathin CoSe2 Nanosheets for Water Oxidation. *J. Am. Chem. Soc.* **2014**, *136*, 15670−15675.
(42) Xing, C.; Xie, Z.; Liang, Z.; Liang, W.; Fan, T.; Ponraj, J. S.; Dhanabalan, S. C.; Fan, D.; Zhang, H. 2D Nonlayered Selenium Nanosheets: Facile Synthesis, Photoluminescence, and Ultrafast Photonics. *Adv. Opt. Mater.* **2017**, *5*, 1700884−1700894.
(43) Xie, Z.; Xing, C.; Huang, W.; Fan, T.; Li, Z.; Zhao, J.; Xiang, Y.; Guo, Z.; Li, J.; Yang, Z.; Dong, B.; Qu, J.; Fan, D.; Zhang, H. Ultrathin 2D Nonlayered Tellurium Nanosheets: Facile Liquid-Phase Exfoliation, Characterization, and Photoresponse with High Performance and Enhanced Stability. *Adv. Funct. Mater.* **2018**, *28*, 1705833.
(44) Brent, J. R.; Lewis, D. J.; Lorenz, T.; Lewis, E. A.; Savjani, N.; Haigh, S. J.; Seifert, G.; Derby, B.; O'Brien, P. Tin(II) Sulfide (SnS) Nanosheets by Liquid-Phase Exfoliation of Herzenbergite: IV-VI Main Group Two-Dimensional Atomic Crystals. *J. Am. Chem. Soc.* **2015**, *137*, 12689−12696.
(45) Zhu, K. Y.; Vassel, A.; Brisset, F.; Lu, K.; Lu, J. Nanostructure formation mechanism of α-titanium using SMAT. *Acta Mater.* **2004**, *52*, 4101−4110.
(46) Kurtz, R. L.; Henrich, V. E. Comparison of Ti 2p Core-Level Peaks from TiO2, Ti2O3, and Ti Metal, by XPS. *Surf. Sci. Spectra* **1998**, *5*, 179−181.
(47) Sul, Y.-T.; Johansson, C. B.; Petronis, S.; Krozer, A.; Jeong, Y.; Wennerberg, A.; Albrektsson, T. Characteristics of the surface oxides on turned and electrochemically oxidized pure titanium implants up to dielectric breakdown: *Biomaterials* **2002**, *23*, 491.
(48) Gonçalves, J. E.; Castro, S. C.; Ramos, A. Y.; Alves, M. C. M.; Gushikem, Y. X-ray absorption and XPS study of titanium mixed oxides synthesized by the sol-gel method. *J. Electron Spectrosc. Relat. Phenom.* **2001**, *114−116*, 307−311.
(49) Galvanetto, E.; Galliano, F. P.; Borgioli, F.; Bardi, U.; Lavacchi, A. XRD and XPS study on reactive plasma sprayed titanium-titanium nitride coatings. *Thin Solid Films* **2001**, *384*, 223−229.
(50) Nemanich, R. J.; Tsai, C. C.; Connell, G. A. N. Interference-Enhanced Raman Scattering of Very Thin Titanium and Titanium Oxide Films. *Phys. Rev. Lett.* **1980**, *44*, 273−276.
(51) Balachandran, U.; Eror, N. G. Raman Spectra of Titanium Dioxide. *J. Solid State Chem.* **1982**, *42*, 276−282.
(52) Sakai, N.; Fujishima, A.; Watanabe, T.; Hashimoto, K. Quantitative Evaluation of the Photoinduced Hydrophilic Conversion Properties of TiO2Thin Film Surfaces by the Reciprocal of Contact Angle. *J. Phys. Chem. B* **2003**, *107*, 1028−1035.
(53) Sakai, N.; Wang, R.; Fujishima, A.; Watanabe, T.; Hashimoto, A. Effect of Ultrasonic Treatment on Highly Hydrophilic TiO2 Surfaces. *Langmuir* **2012**, *14*, 5918−5920.
(54) Robinson, J. T.; Tabakman, S. M.; Liang, Y.; Wang, H.; Sanchez Casalongue, H.; Vinh, D.; Dai, H. Ultrasmall Reduced Graphene Oxide with High near-Infrared Absorbance for Photothermal Therapy. *J. Am. Chem. Soc.* **2011**, *133*, 6825−6831.
(55) Liu, T.; Wang, C.; Gu, X.; Gong, H.; Cheng, L.; Shi, X.; Feng, L.; Sun, B.; Liu, Z. Drug Delivery with PEGylated MoS2Nano-sheets for Combined Photothermal and Chemotherapy of Cancer. *Adv. Mater.* **2014**, *26*, 3433−3440.
(56) Cheng, L.; Liu, J.; Gu, X.; Gong, H.; Shi, X.; Liu, T.; Wang, C.; Wang, X.; Liu, G.; Xing, H.; Bu, W.; Sun, B.; Liu, Z. PEGylated WS2Nanosheets as a Multifunctional Theranostic Agent for in vivo Dual-Modal CT/Photoacoustic Imaging Guided Photothermal Therapy. *Adv. Mater.* **2014**, *26*, 1886−1893.
(57) Sun, Z.; Xie, H.; Tang, S.; Yu, X.-F.; Guo, Z.; Shao, J.; Zhang, H.; Huang, H.; Wang, H.; Chu, P. K. Ultrasmall Black Phosphorus Quantum Dots: Synthesis and Use as Photothermal Agents. *Angew. Chem., Int. Ed.* **2015**, *54*, 11526−11530.
(58) Lin, H.; Gao, S.; Dai, C.; Chen, Y.; Shi, J. A Two-Dimensional Biodegradable Niobium Carbide (MXene) for Photothermal Tumor Eradication in NIR-I and NIR-II Biowindows. *J. Am. Chem. Soc.* **2017**, *139*, 16235−16247.
(59) Ding, X.; Liow, C. H.; Zhang, M.; Huang, R.; Li, C.; Shen, H.; Liu, M.; Zou, Y.; Gao, N.; Zhang, Z.; Li, Y.; Wang, Q.; Li, S.; Jiang, J. Surface Plasmon Resonance Enhanced Light Absorption and Photothermal Therapy in the Second near-Infrared Window. *J. Am. Chem. Soc.* **2014**, *136*, 15684−15693.
(60) Tsai, M.-F.; Chang, S.-H. G.; Cheng, F.-Y.; Shanmugam, V.; Cheng, Y.-S.; Su, C.-H.; Yeh, C.-S. Au Nanorod Design as Light-Absorber in the First and Second Biological near-Infrared Windows for in Vivo Photothermal Therapy. *ACS Nano* **2013**, *7*, 5330.
(61) Roper, D. K.; Ahn, W.; Hoepfner, M. Microscale Heat Transfer Transduced by Surface Plasmon Resonant Gold Nanoparticles. *J. Phys. Chem. C* **2007**, *111*, 3636−3641.
(62) Wang, B.; Wang, J.-H.; Liu, Q.; Huang, H.; Chen, M.; Li, K.; Li, C.; Yu, X.-F.; Chu, P. K. Rose-Bengal-Conjugated Gold Nanorods for in Vivo Photodynamic and Photothermal Oral Cancer Therapies. *Biomaterials* **2014**, *35*, 1954−1966.
(63) Hessel, C. M.; Pattani, V. P.; Rasch, M.; Panthani, M. G.; Koo, B.; Tunnell, J. W.; Korgel, B. A. Copper Selenide Nanocrystals for Photothermal Therapy. *Nano Lett.* **2011**, *11*, 2560−2566.

DOI: 10.1021/acsami.9b04628
ACS Appl. Mater. Interfaces 2019, 11, 22129−22140

(64) Yin, W.; Yan, L.; Yu, J.; Tian, G.; Zhou, L.; Zheng, X.; Zhang, X.; Yong, Y.; Li, J.; Gu, Z.; Zhao, Y. High-Throughput Synthesis of Single-Layer MoS2 Nanosheets as a near-Infrared Photothermal-Triggered Drug Delivery for Effective Cancer Therapy. *ACS Nano* **2014**, *8*, 6922.
(65) Xie, Z.; Wang, D.; Fan, T.; Xing, C.; Li, Z.; Tao, W.; Liu, L.; Bao, S.; Fan, D.; Zhang, H. Black Phosphorus Analogue Tin Sulfide Nanosheets: Synthesis and Application as near-Infrared Photothermal Agents and Drug Delivery Platforms for Cancer Therapy. *J. Mater. Chem. B* **2018**, *6*, 4747−4755.
(66) Tao, W.; Ji, X.; Xu, X.; Islam, M. A.; Li, Z.; Chen, S.; Saw, P. E.; Zhang, H.; Bharwani, Z.; Guo, Z.; et al. Antimonene Quantum Dots: Synthesis and Application as Near-Infrared Photothermal Agents for Effective Cancer Therapy. *Angew. Chem., Int. Ed.* **2017**, *56*, 11896−11900.
(67) Lee, C.; Hong, C.; Kim, H.; Kang, J.; Zheng, H. M. TiO2 Nanotubes as a Therapeutic Agent for Cancer Thermotherapy. *Photochem. Photobiol.* **2010**, *86*, 981−989.
(68) Hong, C.; Kang, J.; Lee, J.; Zheng, H.; Hong, S.; Lee, D.; Lee, C. Photothermal Therapy Using TiO2 Nanotubes in Combination with Near-Infrared Laser. *J. Cancer Ther.* **2010**, *01*, 52−58.
(69) Ni, W.; Li, M.; Cui, J.; Xing, Z.; Li, Z.; Wu, X.; Song, E.; Gong, M.; Zhou, W. 808 nm light triggered black TiO2 nanoparticles for killing of bladder cancer cells. *Mater. Sci. Eng., C* **2017**, *81*, 252.

DOI: 10.1021/acsami.9b04628
ACS Appl. Mater. Interfaces 2019, 11, 22129−22140